IWSCFF 2022

Fast Angles-Only Relative Navigation Using Polynomial Dynamics

Matthew Willis* **and Simone D'Amico†**

A fast and efficient method for initial relative orbit determination from bearing-angle measurements is introduced. The range ambiguity problem for angles-only relative navigation is addressed by modeling nonlinear effects with a novel second-order mapping from relative orbit elements (ROE) to relative position coordinates. This model is used to form a system of polynomial constraint equations linking the line-of-sight measurements to the ROE. An efficient method for solving this system is developed around the insight that the ROE scale with the ratio of the inter-spacecraft separation to the orbit radius and are therefore small for most applications of interest. The method uses a truncated expansion of the quadratic formula to recursively eliminate unknowns, reduce the dimension of the system, and ultimately acquire an approximate solution. Strategies for improving robustness, efficiency, and accuracy are developed and the method is applied to general second-order systems as well as to a broad range of IROD scenarios. Modifications to the constraint equations and solution algorithm are introduced to address the challenge of bias in the bearing-angle measurements.

keywords: Vision-based Navigation, Modelling and Param. of Relative Dynamics, Nonlinear filtering

1. Introduction

Rapid growth in the population of satellites orbiting Earth poses challenges for space situational awareness while driving demand for increasingly autonomous navigation systems. Similarly, the increased density of valuable space assets is advancing the need for on-orbit servicing and debris removal technologies. These trends give rise to the problem of identifying the orbital state of a space resident object using measurements taken by an observer spacecraft, potentially without cooperation or prior knowledge of the target's state. While many sensor and measurement combinations could be applied to this Initial Relative Orbit Determination (IROD) problem, bearing-angle measurements from a single camera are a particularly attractive option due to the ubiquity, passivity, modest price, and small form factor of camera sensors. A major challenge for angles-only relative navigation is the weak observability of the state, first elaborated by Woffinden. [1] Linear relative position models, including Clohessy-Wiltshire (CW) and Yamanaka-Ankersen (YA) as well as linear mappings from relative orbit elements (ROE) or orbit element differences to the translational coordinates, lead to ambiguity in the range between the observer spacecraft and the target. [2–5] The relative state can only be resolved to within an unknown scale factor because any range value would produce the same set of bearing-angle measurements from the linear system. This paper explores the use of a second-order dynamics model to capture the nonlinear range behavior and an efficient algorithm for solving the resulting system of polynomial constraint equations for the relative state.

Several strategies for circumventing the range ambiguity have been proposed in the literature. One is to maneuver the observer to effectively obtain stereoscopic information, offset in time. [6] This approach is undesirable due to the consumption of valuable fuel and the logistical complexity of maneuver planning. Another approach is to offset the camera from the observer spacecraft's center of mass and use attitude maneuvers to achieve a similar outcome without consuming fuel. [7] The drawback is that structural mass must be added to achieving the large baseline needed for range resolution, and attitude maneuvers bring their own logistical difficulties. More favorable strategies seek to capture the range information in the dynamics model. This can be accomplished by changing the coordinate system or state representation. Woffinden's dilemma applies specifically to linear models in Cartesian coordinates, but it has been shown that the relative state is observable for linear models in curvilinear coordinates. [8] One may also use the exact, nonlinear transformations between ROE and relative position coordinates to connect an orbital element state to the line-of-sight measurements. [9,10] A major advantage of this approach is the ability to incorporate effects from perturbations

*PhD Candidate in Aeronautics and Astronautics, Stanford University, United States, mbwillis@stanford.edu

†Associate Professor of Aeronautics and Astronautics, Stanford University, United States, damicos@stanford.edu

such as Earth oblateness, solar radiation pressure, and atmospheric drag through linear models in the ROE space. [11, 12] However, this method relies on batch least-squares initialization using measurements spanning more than a full orbit. [13] The present work adopts an intermediate approach, using a new, second-order mapping from ROE to relative position coordinates. The range ambiguity is resolved by the incorporation of nonlinear effects, while the use of an ROE representation allows for the modeling of perturbations. Although solving the nonlinear system is computationally challenging, this approach can potentially give a coarse initialization from a small number of measurements taken over a fraction of an orbit.

Higher-order models for spacecraft relative motion have been studied since the introduction by London of the approximate second-order solution for near-circular orbits. [14] Having been independently derived multiple times, this second-order solution is commonly referred to as the Quadratic Volterra (QV) model. [15–17] Melton used an approximation technique similar to that of London to incorporate the effect of small eccentricities into a closed-form solution. [18] This technique has been refined and extended by Butcher and others to develop families of second- and third-order solutions incorporating small eccentricity effects as well as the leading-order effect of Earth oblateness. [19, 20] All of these models are explicit in time, but are based on the same near-circular-orbit assumption as CW and are therefore limited in their applicability. Willis, Lovell, and D'Amico (WLD) circumvented this limitation by extending the YA model into a second-order solution that is applicable to arbitrarily eccentric orbits. [21] Past studies of IROD using higher-order dynamics have focused on the QV and WLD models, both of which were derived as solutions to the equations of relative motion. [22, 23] Both of these models are based on approximate solutions to the equations of relative motion. An alternative modeling strategy is to approximate the geometric transformation from an orbital element description that is exact for Keplerian motion. Linear mappings derived in this manner are analogous to the CW and YA solutions in their respective orbit regimes, and commonplace in the literature. [24] One innovation of the present work is the introduction of a second-order mapping from ROE to relative position coordinates, and its use in forming a system of polynomial constraint equations for angles-only IROD.

Unlike linear systems, higher-order polynomial systems do not have general analytical solutions. Their solutions are typically represented algebraically or computed numerically using specialized algorithms. A standard algebraic representation is a triangular decomposition into regular chains, which is analogous to Gaussian elimination of linear systems into row-echelon form. [25] However, the latter terminates in a solution for the final variable which can be back-substituted to obtain the solutions for all variables in the system. Triangular decomposition of a polynomial system terminates in a univariate polynomial of high degree. In principle, the solution of this univariate polynomial can be substituted into the second equation in the chain, producing a univariate equation that can be solved for the second variable, and this process repeated to obtain all solutions to the system. Because the Abel-Ruffini theorem precludes the existence of solutions to polynomials of degree five or higher in terms of radicals, each of these solutions must be obtained using numerical root-finding algorithms. [26] While regular chains provide a powerful tool for representing the exact solution to a system of algebraic equations, they do not in general provide an efficient path to a numerical solution. Newman et al. discuss several numerical strategies for finding polynomial roots in the context of IROD, ultimately adopting one based on Macaulay resultant theory. [27] More recent work by the authors and others applied the method of homotopy continuation, which is considered the state of the art for solving systems of polynomial equations. [23, 28] This approach finds roots by smoothly transforming a system with known solutions into the target system. [29] Although this method is robust, it requires expensive numerical integration of a high-dimensional state through complex space, and is not practical for implementation on flight processors. The second major innovation of this work is the application of an efficient strategy for finding approximate solutions which are suitable for the IROD problem.

The next section introduces the polynomial measurement equations for IROD and the second-order dynamics model. This is followed in Section 3 by the introduction of an efficient solution algorithm based on second-order approximations. The derivation of the core equations is accompanied by a discussion of strategies to improve robustness, reduce computational cost, and increase the accuracy of the resulting solution. Mathematical validation of the algorithm is provided through testing on randomly generated polynomial systems with known solutions. The algorithm is then applied to the IROD problem in Section 4. Prescribed example problems in near-circular

and highly-elliptical orbit are used to demonstrate its qualitative performance, while a quantitative assessment is obtained from a large set of scenarios drawn from the relative state domain of interest. A modified version of the approach is then developed and tested for the case in which an error in the observer's state knowledge adds bias to the measurements. Finally, the paper concludes with a review of the most important findings and outlook on future research paths.

2. Angles-Only Initial Relative Orbit Determination

2.1 *Problem Formulation*

The IROD problem studied in this work entails estimating the relative state of a target spacecraft from a series of observations with a monocular camera. The measurements therefore consist of pairs of bearing angles to the target in the camera frame at known instants in time. These can be mapped to unit vectors in the observer's radial-transverse-normal (RTN)—also called the local-vertical local-horizontal frame—given its orbital state, attitude, and configuration. This work assumes that the relevant parameters are available from the observer's attitude and orbit determination system. It also neglects the problem of target identification and tracking, which is addressed elsewhere in the literature. [30, 31] Consequently, the inputs to the IROD problem under consideration are line-of-sight unit vectors expressed in the observer's RTN frame,

$$\hat{\boldsymbol{\ell}} = \begin{bmatrix} \ell_x \\ \ell_y \\ \ell_z \end{bmatrix} \qquad [1]$$

The basis vectors for the RTN frame are $\hat{\mathbf{x}}$, $\hat{\mathbf{y}}$, and $\hat{\mathbf{z}}$, where $\hat{\mathbf{x}}$ is directed radially away from the central body, $\hat{\mathbf{z}}$ is parallel with the observer's orbital angular momentum vector, and $\hat{\mathbf{y}} = \hat{\mathbf{z}} \times \hat{\mathbf{x}}$ completes the right-handed triad.

A mathematical relationship between the measurements and the relative state parameters is established by the fact that the line-of-sight vector $\hat{\boldsymbol{\ell}}$ must be parallel with the relative position vector $\boldsymbol{\delta}\mathbf{r} = \mathbf{r}_t - \mathbf{r}$. Because the observer is at the origin of the RTN coordinate system, the relative position vector is conveniently expressed therein as $\boldsymbol{\delta}\mathbf{r} = [x, y, z]^T$. To make dynamics modeling more convenient for eccentric orbits, the relative position coordinates are normalized by the observer's orbit radius to form the nondimensional vector $\boldsymbol{\delta}\bar{\mathbf{r}} = \boldsymbol{\delta}\mathbf{r}/r = [\bar{x}, \bar{y}, \bar{z}]^T$. This scalar transformation does not affect the vector's orientation, so a set of constraint equations is obtained from the null cross product of the line-of-sight vector and scaled relative position vector at a given point in time,

$$\hat{\boldsymbol{\ell}} \times \boldsymbol{\delta}\bar{\mathbf{r}} = \begin{bmatrix} \ell_z\bar{y} - \ell_y\bar{z} \\ \ell_x\bar{z} - \ell_z\bar{x} \\ \ell_y\bar{x} - \ell_x\bar{y} \end{bmatrix} = \begin{bmatrix} 0 \\ 0 \\ 0 \end{bmatrix} \qquad [2]$$

Because any of the three resulting equations can be obtained by subtracting the other two, each observation provides only two linearly independent constraints. The relative state has six degrees of freedom, so measurements from at least three observation times must be combined to form the six constraint equations needed to fully determine the system. This paper uses the second and third relations in Equation 2, neglecting the first relation.

The relative state is characterized in general by a set of six constant parameters. These could equivalently be cast as initial conditions of relative position and velocity, combinations of orbital elements, or integration constants of a solution to the governing differential equations. This work represents a general set of relative state constants by the vector $\mathbf{c}$ and models the relative position coordinates as second-order polynomials with the form

$$\begin{aligned} \bar{x} &= \mathbf{b}_x^T(\theta)\,\mathbf{c} + \mathbf{c}^T B_x(\theta)\,\mathbf{c} \\ \bar{y} &= \mathbf{b}_y^T(\theta)\,\mathbf{c} + \mathbf{c}^T B_y(\theta)\,\mathbf{c} \\ \bar{z} &= \mathbf{b}_z^T(\theta)\,\mathbf{c} + \mathbf{c}^T B_z(\theta)\,\mathbf{c} \end{aligned} \qquad [3]$$

The vectors $\mathbf{b}_i \in \mathbb{R}^6$ contain the coefficients of the terms that are linear in the relative state constants and the matrices $B_i \in \mathbb{R}^{6\times 6}$ contain the coefficients of the second-order terms. These coefficients capture the time-variation of the relative position coordinates, indicated by their explicit dependence on the observer's true argument of latitude $\theta = \omega + f$, where ω is the argument of perigee and f is the true anomaly. Further details concerning the choice of state parameters and the dynamics model will be discussed in Section 2.2. Figure 1 visualizes the IROD problem for a near-circular orbit scenario. The target's relative trajectory in the observer's RTN frame is shown in black while the lines of sight at the three measurement times are shown in blue. The trajectory in red is the motion predicted by the polynomial dynamics model using the estimated relative state.

The range ambiguity problem for linear dynamics models can be made mathematically clear by combining Equations 2 and 3 and dropping the second-order terms from the latter. The relative position vector is approximated by $\boldsymbol{\delta}\bar{\mathbf{r}} = [\mathbf{b}_x, \mathbf{b}_y, \mathbf{b}_z]^T\mathbf{c}$, and the con-

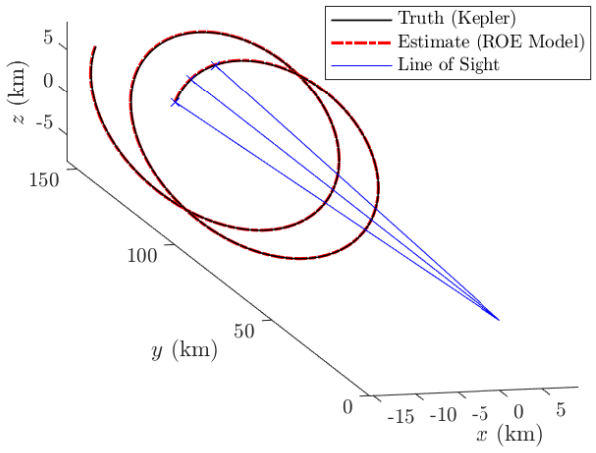

Fig. 1: Depiction of angles-only IROD from three line-of-sight measurements in near-circular orbit, including true relative trajectory and prediction from estimated relative state.

straint equations become

$$\begin{aligned}
{}^{1}\mathbf{p}^{T}\mathbf{c} &= \left[\ell_{1,z}\mathbf{b}_x^T(\theta_1) - \ell_{1,x}\mathbf{b}_z^T(\theta_1)\right]\mathbf{c} = 0 \\
{}^{2}\mathbf{p}^{T}\mathbf{c} &= \left[\ell_{1,y}\mathbf{b}_x^T(\theta_1) - \ell_{1,x}\mathbf{b}_y^T(\theta_1)\right]\mathbf{c} = 0 \\
{}^{3}\mathbf{p}^{T}\mathbf{c} &= \left[\ell_{2,z}\mathbf{b}_x^T(\theta_2) - \ell_{2,x}\mathbf{b}_z^T(\theta_2)\right]\mathbf{c} = 0 \\
&\vdots \\
{}^{6}\mathbf{p}^{T}\mathbf{c} &= \left[\ell_{3,y}\mathbf{b}_x^T(\theta_3) - \ell_{3,x}\mathbf{b}_y^T(\theta_3)\right]\mathbf{c} = 0
\end{aligned} \quad [4]$$

Note that ${}^{i}\mathbf{p} \in \mathbb{R}^6$ are indexed over the constraint equations while θ_j and the corresponding $\hat{\boldsymbol{\ell}}_j$ are indexed over the measurement times. Introducing the matrix $L = [{}^{1}\mathbf{p}, ..., {}^{6}\mathbf{p}]^T$, Equation 4 is more compactly written as

$$L\,\mathbf{c} = 0 \quad [5]$$

It is evident in this form that the relative state constant vector $\mathbf{c} \in \mathbb{R}^6$ defines the null space of the constraint matrix $L \in \mathbb{R}^{6\times6}$. Consequently, scaling $\mathbf{c}$ by any value will result in a valid solution to Equation 5. Similarly, since the relative position coordinates are linearly related to the state parameters in this case, scaling $\mathbf{c}$ is equivalent to scaling the separation between observer and target.

If the full, second-order relative dynamics model of Equation 3 is used, the constraints form polynomial equations which can be expressed in terms of the linear coefficient vector ${}^{i}\mathbf{p}$ and quadratic coefficient matrix ${}^{i}P$ as

$${}^{i}\mathbf{p}^{T}\mathbf{c} + \mathbf{c}^{T}\,{}^{i}P\,\mathbf{c} = 0 \quad [6]$$

Using the constraint ordering adopted for the linear case in Equation 4, the polynomial coefficients are given by

$${}^{i}\mathbf{p} = \begin{cases} \ell_{z,j}\mathbf{b}_y(\theta_j) - \ell_{y,j}\mathbf{b}_z(\theta_j) & i = 1,3,5 \\ \ell_{x,j}\mathbf{b}_z(\theta_j) - \ell_{z,j}\mathbf{b}_x(\theta_j) & i = 2,4,6 \end{cases} \quad [7]$$

$${}^{i}P = \begin{cases} \ell_{z,j}B_y(\theta_j) - \ell_{y,j}B_z(\theta_j) & i = 1,3,5 \\ \ell_{x,j}B_z(\theta_j) - \ell_{z,j}B_x(\theta_j) & i = 2,4,6 \end{cases} \quad [8]$$

$$j = \begin{cases} (i+1)/2 & i = 1,3,5 \\ i/2 & i = 2,4,6 \end{cases} \quad [9]$$

Because B_x, B_y, and B_z appear only as quadratic forms in Equation 3, they may be assumed upper triangular without loss of generality. According to Equation 7, this property would extend to ${}^{i}P$. A few additional notation choices merit elaboration at this stage to avoid confusion. The vector $\mathbf{c}$ contains the constant relative state parameters we wish to determine. The coefficients appearing in the vectors $\mathbf{b}_x$, $\mathbf{b}_y$, and $\mathbf{b}_z$, and the matrices B_x, B_y, and B_z are written explicitly as functions of θ to emphasize that they are computed from a mathematical model. Conversely, the line-of-sight vectors $\hat{\boldsymbol{\ell}}_j$ represent measured quantities and are labeled with subscripts that identify the corresponding measurement time. The polynomial constraint coefficients in ${}^{i}\mathbf{p}$ and ${}^{i}P$ combine the line-of-sight measurements with the dynamics model coefficients computed at the corresponding times. Their implicit time-dependence is dropped in favor of the index i, which highlight their role in a system of equations to be solved for the relative state constants $\mathbf{c}$. This indexing choice also provides greater flexibility for later modification of the definitions in Equation 7. Recall that those follow from the arbitrary selection and ordering of two out of the three constraint relationships in Equation 2, as well as the assumption that the minimum number of measurements required to determine the six-dimensional state are being used.

Equation 6 represents the IROD problem as a system of polynomials to be solved for the state constants $\mathbf{c}$. While the linear formulation in Equation 4 with full-rank L leads to a solution vector with indefinite magnitude, polynomial systems lead to multiple definite solutions that may be real or complex. Bézout's theorem gives the maximum possible number of solutions, stating that a system of β equations of degree α has α^{β} solutions. [32] If none of the

matrices ${}^{i}P$ appearing in Equation 6 are null, there are $\beta = 6$ equations with degree $\alpha = 2$, resulting in $2^6 = 64$ possible solutions. Many of these roots will be complex, but the relative state constant vector $\mathbf{c}$ must be real. However, the complex solutions cannot be rejected outright. The dynamics model in Equation 3 is only an approximation of the relative motion, so the line-of-sight directions will not correspond exactly with the predicted relative position vectors, even if observer state uncertainty, non-Keplerian forces, and measurement errors are absent. Consequently, the closest solution of Equation 6 to the true relative state may have small imaginary components. Because the polynomial coefficients are real, any complex solutions must occur in conjugate pairs, so considering only the real parts may reduce the number of relevant solution candidates substantially. Practical physical considerations may reduce or resolve the remaining ambiguity.

First, Equation 6 has no degree-zero terms, so must admit the trivial solution $\mathbf{c} = \mathbf{0}$. This may be removed from the set of candidate solutions since it places the target and observer in the same state. Next, the constraint equations require $\hat{\boldsymbol{\ell}}$ and $\boldsymbol{\delta}\bar{\mathbf{r}}$ to lie on the same line, but not to have the same orientation. Thus, some solutions to Equation 2 may produce relative position vectors antiparallel to the line-of-sight vector. Some candidate state estimates $\tilde{\mathbf{c}}$ may be eliminated by checking

$$\boldsymbol{\delta}\bar{\mathbf{r}}(\theta_j, \tilde{\mathbf{c}}) \cdot \hat{\boldsymbol{\ell}}_j > 0 \qquad [10]$$

for θ_j corresponding to each measurement time. In principle, a series of three line-of-sight measurements may lead to eight parallel/antiparallel permutations. However, few of these may arise from admissible solutions to the constraint equations, so the potential reduction of relative state candidates resulting from this test cannot be determined a priori. Perhaps the most important consideration for eliminating candidate solutions is plausibility. For example, candidates that lead to an escape trajectory or one which intersects Earth's surface may be rejected if the target is expected to be in a closed orbit. Lower and upper bounds on the inter-spacecraft separation may be imposed by measurement and dynamics modeling considerations. The details of the relative dynamics model are the subject of section 2.2, but it follows from the form of Equation 3 that the relative state constants will be similar in magnitude to the nondimensional relative position coordinates. Thus, the constants will be less than one for inter-spacecraft separations less than a few thousand kilometers. If all checks fail to reduce the number of candidate solutions to one, the remaining ambiguity may be addressed by comparing IROD results using a different combination of measurements over a longer arc.

2.2 *Relative Dynamics Model*

Much of the work to date on IROD using polynomial dynamics utilized models based on approximate solutions to the second- and third-order expansions of the equations of relative motion in RTN coordinates. Such models are closely related to the well-known CW and YA models, both in their form and derivation methodology, and use the integration constants of those models as the relative state parameters. Previous work on this topic by the authors used the WLD model, which is a second-order extension of the linear YA model and therefore valid for both circular and eccentric orbits. [23] This model follows the form of Equation 3, with the relative state vector $\mathbf{c}$ denoted in that work by the vector of integration constants $\mathbf{K}$. Although higher-order models in this category are more accurate and apply to larger separations than their linear counterparts, they share fundamental limitations and have their own distinct drawbacks. First, as solutions to an approximation of the relative dynamics, their accuracy degrades over time. This is true regardless of approximation order. Higher-order solutions improve the accuracy for a given spatial configuration, but under most circumstances they merely slow the steady growth in propagation error over time. The second problem that beleaguers higher-order models stems from their method of derivation. Because general solutions for systems of higher-order differential equations are not available, these models are usually created from the linear solutions using approximation techniques. As a result, they do not constitute stand-alone solutions with their own intrinsic set of integration constants. They are more accurately viewed as corrections to the linear solutions, with additional degrees of freedom fixed by arbitrary choices on the part of the astrodynamicist—usually that the corrections vanish at some reference time. A relative state determined from a model thus derived has limited value independent of the model.

One way that the present work distinguishes itself from earlier IROD studies is through the introduction and utilization of a new second-order model based on the quasi-nonsingular ROE. The relative state constant vector $\mathbf{c}$ adopted for this work is the set of ROE

$\boldsymbol{\delta\alpha}$ defined by

$$\boldsymbol{\delta\alpha} = \begin{bmatrix} \delta a \\ \delta\lambda \\ \delta e_x \\ \delta e_y \\ \delta i_x \\ \delta i_y \end{bmatrix} = \begin{bmatrix} (a_t - a)/a \\ (u_t - u) + (\Omega_t - \Omega)\cos i \\ e_t \cos\omega_t - e\cos\omega \\ e_t \cos\omega_t - e\sin\omega \\ i_t - i \\ (\Omega_t - \Omega)\sin i \end{bmatrix} \quad [11]$$

where $\boldsymbol{\alpha} = [a, e, i, \Omega, \omega, M]^T$ are the classical Keplerian elements and $u = \omega + M$ is the mean argument of latitude. As elsewhere in this paper, quantities relating to the target spacecraft are labeled with a subscript t while those without a subscript relate to the chief. Use of the eccentricity vector components $e_x = e\cos\omega$ and $e_y = e\sin\omega$ in this parameterization avoids singularities for circular orbits. However, $\boldsymbol{\delta\alpha}$ is not uniquely defined if the target spacecraft is in an equatorial orbit and is therefore deemed quasi-nonsingular.

The ROE are related to the relative position vector $\boldsymbol{\delta r}$ in RTN through a series of nonlinear transformations. First the target's orbital elements are obtained by combining the ROE with the observer's orbital elements $\boldsymbol{\alpha}$. The two sets of orbital elements allow computation of the two spacecraft's position vectors in Earth-Centered Inertial (ECI) coordinates. These are then rotated and subtracted to yield the relative position vector in the observer's RTN frame. The sequence of transformations and dependencies is summarized by

$$\begin{aligned} \{\, \boldsymbol{\alpha}, \boldsymbol{\delta\alpha} \,\} \rightarrow \{\, \boldsymbol{\alpha}, \boldsymbol{\alpha}_t(\boldsymbol{\alpha}, \boldsymbol{\delta\alpha}) \,\} \rightarrow \\ \{\, \mathbf{r}(\boldsymbol{\alpha}), \mathbf{r}_t(\boldsymbol{\alpha}_t) \,\}_{ECI} \rightarrow \{\, \mathbf{r}(\boldsymbol{\alpha}), \mathbf{r}_t(\boldsymbol{\alpha}_t) \,\}_{RTN} \\ \rightarrow \{\, \boldsymbol{\delta r}(\mathbf{r}, \mathbf{r}_t) \,\}_{RTN} \end{aligned} \quad [12]$$

Condensed into a single equation, the sequence becomes

$$\begin{aligned} \boldsymbol{\delta r} = R_{RTN}^{ECI}(\boldsymbol{\alpha}) R_{ECI}^{RTN,t}(\boldsymbol{\alpha}, \boldsymbol{\delta\alpha}) \big[\mathbf{r}_t(\boldsymbol{\alpha}, \boldsymbol{\delta\alpha})\big]_{RTN,t} \\ - \big[\mathbf{r}(\boldsymbol{\alpha})\big]_{RTN} \end{aligned} \quad [13]$$

where $R_{ECI}^{RTN,t}$ is the rotation matrix from the target's RTN coordinates to ECI, and R_{RTN}^{ECI} is from ECI to the observer's RTN coordinates. Recall that a spacecraft's position vector is conveniently expressed in its own RTN coordinates as $[\mathbf{r}]_{RTN} = [r, 0, 0]^T$. While the matrix and vector operations in Equation 13 are linear, the rotations and orbit radii involve products, trigonometric functions, and inverse functions of the ROE. To obtain a mapping from $\mathbf{c} = \boldsymbol{\delta\alpha}$ to $\boldsymbol{\delta\bar{r}}$ in the form of Equation 3, these nonlinearities must be expanded and truncated at second order in the relative state constants. The details of this procedure are beyond the scope of this paper, but a detailed statement of the resulting model coefficients is presented in the Appendix.

Care was taken in the derivation of the new, second-order ROE-to-RTN mapping to avoid singularities near zero eccentricities, so like the WLD model and quasi-nonsingular ROE, it is applicable to observer orbits of any eccentricity. Whereas higher-order models like QV and WLD solve an approximation of the relative motion dynamics, the new mapping approximates an exact description of the Keplerian relative motion geometry. While this distinction may seem semantic, it has major implications for the model's accuracy and utility. First, the approximation of an exact solution is more stable over time than an approximation of the underlying dynamics. Given accurate initial conditions, the new model and WLD would give comparable propagation errors over one orbit. However, WLD's dynamical approximation would lead to errors that grow over time while the new model's geometric approximation would lead to errors that effectively repeat from orbit to orbit. More importantly, the new model's state constants are the ROE, whose physical and geometric significance follow from their definition in Equation 11 and are independent of the form of the model itself. For example, the ROE outputs of the IROD methodology proposed herein would be immediately useful in many guidance, navigation, and control algorithms from the large body of ROE literature. Similarly, the new mapping could be readily combined with existing state transition matrices that linearly approximate the effects of perturbations such as atmospheric drag, J_2, third-body effects, and solar radiation pressure on the ROE. [11, 12] At this stage, all pieces needed to construct the system of polynomial constraints in Equations 6 and 7 have been introduced. The subsequent sections will address methods for finding a solution to the angles-only IROD problem.

3. Quadratic Formula Approximation

3.1 *Motivation*

As formulated in Section 2.1, the IROD problem entails solving a system of six second-order equations in the six relative state constants $\mathbf{c}$, chosen herein to be the quasi-nonsingular ROE $\boldsymbol{\delta\alpha}$. The methods of homotopy continuation and regular chains are powerful tools for solving general polynomial systems, but

come at an impractical computational cost for onboard implementation. A more efficient approach has been derived for this problem by taking advantage of three insights:

1. The equations are quadratic.
2. Their solutions will be inexact.
3. Their solutions will be small.

The first is a consequence of the linearity of Equation 2 in the relative position coordinates and the choice of a second-order dynamics model in Equation 3. A quadratic equation in one unknown has the form

$$p_0 + p_1 c_1 + p_{11} c_1^2 \qquad [14]$$

and its two solutions are given by the well-known quadratic formula,

$$c_{1\pm} = \frac{1}{2\,p_{11}} \left(-\,p_1 \pm \sqrt{p_1^2 - 4\,p_{11}\,p_0} \right) \qquad [15]$$

Any equation in the IROD constraint system could be solved for one of the relative state constants in terms of the remaining constants. However, this solution involves radicals and cannot be combined with the other equations without altering their polynomial character. The second insight reflects the approximate nature of the relative dynamics model. Even in the absence of measurement errors and perturbing forces, the second-order model is an approximation of the Keplerian relative motion. Thus, the polynomial system in Equations 6 and 7 are imperfect representations of the true constraints in Equation 2. Its solution will similarly be an imperfect estimate of the true relative state. From a practical standpoint, this means that the constraint equations do not need to be solved to the high numerical precision typical of polynomial system solvers.

The key to combining the first two insights and unlocking the proposed approach is provided by the third fact: the relative state constants will be small. This follows from the fact that, in accordance with Equation 3, the largest ROE will be comparable in magnitude to the ratio of the inter-spacecraft separation to the observer's orbit radius. Because the latter is bounded below by the radius of the Earth, the inter-spacecraft separation must be on the order of thousands of kilometers for the magnitude of the ROE to approach unity. For applications with 10s of kilometers of separation, the relative state constants are expected to be smaller than 10^{-2}. Consequently, the radical appearing in the quadratic formula may be expanded as a rapidly-converging series about the origin. This leads to a polynomial expression for one constant, which can be used to eliminate it from the remaining equations. By truncating the resulting higher-order terms, the quadratic nature of the remaining equations is preserved at a small cost in accuracy. The process repeats until a numerical value is obtained for the final variable, then back-substituted to find the others. The resulting set of constants will only approximate the true solution of the system, but a good approximation in this context is as valuable as an exact solution. The remainder of this section elaborates the mathematical details of the approach and simple modifications to improve its robustness.

3.2 *Derivation*

In this section, the angles-only IROD problem is replaced with the more general problem of solving a system of N quadratic equations in N unknowns. One of these equations may generally be written as

$$p_0 + \mathbf{p}^T \mathbf{c} + \mathbf{c}^T P \mathbf{c} = 0 \qquad [16]$$

where p_0 is a scalar constant, $\mathbf{p} = [\,p_1, ..., \,p_N]^T$ is a vector containing the coefficients of the first-order terms, and the matrix

$$P = \begin{bmatrix} p_{11} & \cdots & p_{1N} \\ \vdots & \ddots & \vdots \\ p_{N1} & \cdots & p_{NN} \end{bmatrix}$$

contains the coefficients of the quadratic terms. Without loss of generality, one may assume that $P_{ij} = 0$ if $i > j$, so the matrix is upper triangular. Equation 16 differs from Equation 6 only by the inclusion of the degree-zero term p_0 and generalization of the domain of $\mathbf{c}$ from $\mathbb{R}^6$ to $\mathbb{R}^N$. Extracting c_N and combining $\mathbf{c}' = [c_1, ..., c_{N\text{-}1}]^T$ with the coefficients, Equation 16 may be rewritten in the form of univariate quadratic Equation 14 as

$$\begin{aligned} &\left(p_0 + \mathbf{p}_{1:N\text{-}1}^T \mathbf{c}' + \mathbf{c}'^T P_{1:N\text{-}1,1:N\text{-}1} \mathbf{c}' \right) \\ &\quad + \left(p_N + P_{1:N\text{-}1,N}^T \mathbf{c}' \right) c_N + p_{NN} c_N^2 = 0 \end{aligned} \qquad [17]$$

Following Equation 15, the solutions for c_N are

$$\begin{aligned} c_{N\pm} = &-\frac{1}{2\,p_{NN}} \left(p_N + P_{1:N\text{-}1,N}^T \mathbf{c}' \right) \\ &\pm \frac{1}{2\,p_{NN}} \Big[\left(p_N + P_{1:N\text{-}1,N}^T \mathbf{c}' \right)^2 - 4\,p_{NN} \big(p_0 \\ &+ \mathbf{p}_{1:N\text{-}1}^T \mathbf{c}' + \mathbf{c}'^T P_{1:N\text{-}1,1:N\text{-}1} \mathbf{c}' \big) \Big]^{1/2} \end{aligned} \qquad [18]$$

No approximations were introduced between Equations 16 and 18, so the latter is an exact solution for c_N in terms of the remaining unknowns $\mathbf{c}' = [c_1, ..., c_{N\text{-}1}]^T$.

If the unknown state parameters c_i are expected to be small, it is reasonable to assume that terms in which they appear are smaller than terms involving the coefficients alone. In particular, pulling the quantity $\sqrt{p_N^2 - 4\,p_{NN}\,p_0}$ out of the radical term leaves an expression of the form $(1+\varepsilon)^{1/2}$. If the assumption holds, $\varepsilon < 1$ and this expression can be expanded as the binomial series

$$(1+\varepsilon)^{1/2} \approx 1 + \frac{1}{2}\varepsilon - \frac{1}{8}\varepsilon^2 \qquad [19]$$

Dropping terms from ε^2 that are higher than second-order in the unknown state parameters $\mathbf{c}'$, the solutions for c_N can be written approximately as

$$c_{N\pm} \approx d_{0\pm} + \mathbf{d}_\pm^T \mathbf{c}' + \mathbf{c}'^T D_\pm \mathbf{c}' \qquad [20]$$

where the constant, linear, and quadratic coefficients are given by

$$d_{0\pm} = -\frac{p_N}{2\,p_{NN}} \pm \frac{1}{2\,p_{NN}}\sqrt{p_N^2 - 4\,p_{NN}\,p_0} \qquad [21]$$

$$\mathbf{d}_\pm = -\frac{1}{2\,p_{NN}} P_{1:N\text{-}1,N} \pm \frac{1}{\sqrt{p_N^2 - 4\,p_{NN}\,p_0}} \left[\frac{p_N}{2\,p_{NN}} P_{1:N\text{-}1,N} - \mathbf{p}_{1:N\text{-}1}\right] \qquad [22]$$

$$D_\pm = \pm\frac{1}{\sqrt{p_N^2 - 4\,p_{NN}\,p_0}}\Bigg[- P_{1:N\text{-}1,1:N\text{-}1} + \frac{1}{p_N^2 - 4\,p_{NN}\,p_0}\left(p_N\,P_{1:N\text{-}1,N}\mathbf{p}_{1:N\text{-}1}^T - \,p_0\,P_{1:N\text{-}1,N}\,P_{1:N\text{-}1,N}^T - \,p_{NN}\,\mathbf{p}_{1:N\text{-}1}\mathbf{p}_{1:N\text{-}1}^T\right)\Bigg] \qquad [23]$$

Relaxing the assumption that P is upper triangular requires only the replacement of $P_{1:N\text{-}1,N}$ by $\left(P_{1:N\text{-}1,N} + P_{N,1:N\text{-}1}^T\right)$ in Equations 17 through 23.

If values for the remaining state elements $\mathbf{c}' = [c_1, ..., c_{N\text{-}1}]^T$ were known, estimates for c_N could be computed directly from Equation 20. At this stage, its primary utility is that it is a polynomial in the unknowns and can be used to eliminate c_N from the other equations of the system. Suppose one of these equations is

$$q_0 + \mathbf{q}^T\mathbf{c} + \mathbf{c}^T Q\mathbf{c} = 0 \qquad [24]$$

with the assumption $Q_{ij} = 0$ if $i > j$. This assumption can be relaxed by replacing $Q_{1:N\text{-}1,N}$ with $\left(Q_{1:N\text{-}1,N} + Q_{N,1:N\text{-}1}^T\right)$ in the subsequent equations. Rearranging into the form of Equation 17, substituting Equation 20 for c_N, and truncating terms beyond second-order in $\mathbf{c}'$ leads to the reduced equation

$$q_0' + \mathbf{q}'^T\mathbf{c}' + \mathbf{c}'^T Q'\mathbf{c}' = 0 \qquad [25]$$

with modified coefficients

$$q_0' = q_0 + q_N d_{0\pm} + q_{NN} d_{0\pm}^2 \qquad [26]$$

$$\mathbf{q}' = \mathbf{q}_{1:N\text{-}1} + \left(q_N + 2\,q_{NN} d_{0\pm}\right)\mathbf{d}_\pm + d_{0\pm} Q_{1:N\text{-}1,N} \qquad [27]$$

$$Q' = Q_{1:N\text{-}1,1:N\text{-}1} + \left(q_N + 2\,q_{NN} d_{0\pm}\right) D_\pm + \left(Q_{1:N\text{-}1,N} + q_{NN}\mathbf{d}_\pm\right)\mathbf{d}_\pm^T \qquad [28]$$

Whereas Equation 24 was a function of N unknowns, Equation 25 depends on $N-1$. Giving each of the remaining equations the same treatment results in a new system, consisting of $N-1$ quadratic equations in the $N-1$ unknown elements of $\mathbf{c}'$. The new, reduced system is identical in form to the original system, so the process can be repeated with $N \leftarrow N-1$: one equation is solved for one unknown according to Equation 20, then the other equations are reduced according to Equation 25. Eventually the system will be reduced to the univariate quadratic Equation 14, and the value for the terminal unknown is computed from Equation 15. This value can be back-propagated to find the values for the other variables, either using the approximate expression in Equation 20 or the less-approximate form in Equation 18. The latter gives a potentially more accurate solution to the reduced equation at slightly higher computational cost.

A bifurcation occurs at each recursion step according to the choice of $\pm$ in Equation 20. Thus, two sets of coefficients give rise to a pair of reduced systems, just as the quadratic formula yields two solutions. Because the process is repeated N times to arrive at a numerical estimate $\tilde{\mathbf{c}}$, it will form a tree branching into 2^N solution estimates. How this tree may be pruned to avoid excessive computations is addressed later in this section.

3.3 *Pivoting*

In Equations 20 through 28, it was assumed that the last unknown c_N was being eliminated on each recursion, but this may not be optimal. The derivation relies heavily on ε being small in the Binomial series approximation given by Equation 19. Approximation errors will cascade through the recursion tree and large approximations early on will propagate into large errors in the end result. This problem can be mitigated by prioritizing equations and unknowns that are likely to have small approximation errors in the early calculations. This is analogous to the process of pivoting in Gaussian elimination to prevent division by zero and improve numerical stability.

Without prior knowledge of the true values in the solution vector $\mathbf{c}$, the actual approximation error cannot be determined. However, a simple heuristic approach can be used to reduce it in practice. Recall that ε was formed from the ratio of terms involving $\mathbf{c}'$ in Equation 18 to the quantity $\sqrt{p_N^2 - 4\,p_{NN}\,p_0}$. In the case $\mathbf{c}' = \mathbf{0}$, this quantity would be the discriminant of the quadratic polynomial and that nomenclature is adopted henceforth. Although little can be said about the numerator, the size of ε can be reduced by maximizing its denominator. Thus, the proposed heuristic is to solve equation i^* for the unknown parameter j^* such that

$$\{i^*, j^*\} = \underset{i,j}{\operatorname{argmax}} \left({}^{i}p_j^2 - 4\,{}^{i}p_{jj}\,{}^{i}p_0 \right) \qquad [29]$$

where the coefficient indexing convention from Equation 6 has been resumed. It is important to note that for the angles-only IROD constraints in Equation 6, ${}^{i}p_0 = 0$. Its value may change for subsequent recursions according to Equation 26, but at least for the initial step the heuristic simplifies to choosing the $\{i^*, j^*\}$ pair corresponding to the largest value of ${}^{i}p_j$.

To avoid complicating the derivation notation with a non-terminal index, the vector of unknowns $\mathbf{c}$ can be permuted by the matrix A, which is the identity matrix with columns (and rows) j^* and N swapped. The coefficients of the polynomial equations are replaced by

$$\begin{aligned} {}^{i}\mathbf{p} &\leftarrow A\,{}^{i}\mathbf{p} \\ {}^{i}P &\leftarrow A\,{}^{i}P A^T \end{aligned} \qquad [30]$$

for all i. Each recursion step will produce a new permutation matrix, and these may be stacked to restore the original ordering of $\mathbf{c}$.

3.4 *Pruning*

As discussed above, the bifurcation inherent in the recursion leads to a tree culminating in 2^N solution branches. While a system of N quadratic equations has 2^N solutions in general, few of these will correspond to branches of the tree—only those for which the assumption of small $\mathbf{c}$ is valid. The cost of finding the desired solution can be reduced substantially by pruning branches which will lead to invalid estimates. The pruning mechanism is easily understood by introducing a regular structure to the tree. Branches arise from the choice of $\pm$ in Equation 20. Rather than leaving this choice arbitrary, let $\pm$ refer to $\pm\text{sign}(\,p_N)$. It follows from Equation 21 that $+\text{sign}(\,p_N)$ will lead to a value for $d_{0\pm}$ with smaller magnitude than will $-\text{sign}(\,p_N)$. In the special case where $p_0 = 0$, as in the IROD problem under consideration, $d_{0+} = 0$ while $d_{0-} = -\,p_N/\,p_{NN}$. Propagating this sign convention to Equations 26 through 28, one finds that if $q_0 = 0$ and $d_{0+} = 0$, then $q_0' = 0$. Since ${}^{i}p = 0$ for all i in the IROD system, following the $(+)$ branches through the solution tree culminates in the trivial solution $\mathbf{c} = 0$, as shown in Figure 2 It is evident that this is a valid solution for

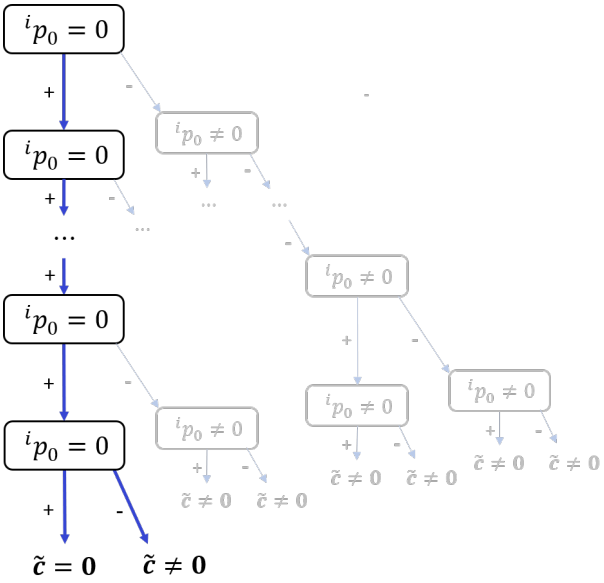

Fig. 2: Recursion tree with $\pm \rightarrow \pm\text{sign}(^{i^*}p_N)$, emphasizing the values of the scalar constants $^{i}p_0$ in the system of equations.

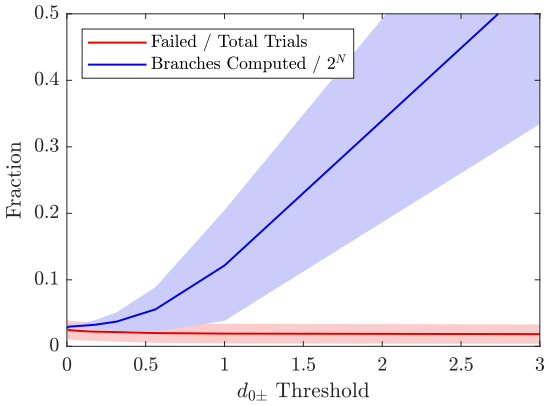

Fig. 3: Failure rate and fraction of branches explored as a function of the pruning threshold d_0^*.

the constraint system in Equation 6, but it is not an interesting one.

According to Equation 20, the value of $d_{0\pm}$ represents the 0^{th}-order estimate of $c_{N\pm}$. If, as assumed, $\mathbf{c}'$ is small, the final estimate for $c_{N\pm}$ will be close to this value. In the case of the IROD problem, all of the d_{0+} will be 0 on the $(+)$ branch of the recursion tree. As Figure 2 illustrates, the adjacent $(-)$ branch leads to a small but nontrivial $\tilde{\mathbf{c}}$. Branches further from the trivial branch will tend to produce larger estimates. Though more difficult to demonstrate, the case $^{i}p_0 \neq 0$ follows a similar pattern. A naive implementation might explore a fixed number of branches around the $(+)$ branch and prune the rest. A more methodical approach is to prune branches if $|d_{0\pm}|$ is above a threshold value d_0^*. A branch corresponding to a value of $d_{0\pm}$ greater than 1 is unlikely to lead to a solution estimate that satisfies the assumptions of the approach.

The choice of d_0^* involves a tradeoff between computational cost and robustness. A higher threshold will prune fewer branches, requiring more computation but potentially capturing more corner cases. Figure 3 demonstrates this tradeoff for 10,000 randomly-generated systems of quadratic equations in six unknowns. The systems were generated with linear and quadratic coefficients randomly drawn from a uniform distribution over $[-10, 10]$. The scalar constants $^{i}p_0$ were computed to satisfy randomly generated solution vectors, the elements of which have logarithmically distributed absolute values less than one. The figure shows the mean and standard deviations for the fraction of branches explored at the given threshold and the fraction of trials which failed to find the specified root. The algorithm was implemented to explore at least the $(+)$ branch in every case, so both the failure rate and fraction of branches pruned approach a limit as d_0^* goes to zero. With this implementation, the failure rate shows little sensitivity to d_0^*, varying from 2.7 ± 1.5 % to 1.8 ± 1.5 % over the tested range. In contrast, the average fraction of branches explored grew from 2.7 ± 0.4 % to 57 ± 22 %. For this six-dimensional system, this is the difference between exploring 1 or 2 branches and exploring up to 50 of the 64 potential branches. Based on these results, $d_0^* = 0.5$ would be a conservative threshold, while a more aggressive implementation could set the value as low as 0.1.

The combined developments of Sections 3.2 to 3.4 form an efficient method for finding Infinitesimal Solutions to Polynomial Equations by Quadratic Truncation and Elimination Recursion (InSPEQTER). Algorithm 1 provides pseudocode for InSPEQTER. Several caveats to this algorithm must be mentioned. In addition to the assumption that the desired solutions will be small, it applies only if $p_{NN} \neq 0$ and the discriminant is nonzero. These restrictions are evident from the presence of these quantities in denominators of Equations 21 through 23. The second-order dynamics model described in Section 2.2 and elaborated in the appendix ensures that these requirements will be met for the angles-only IROD application in

Algorithm 1: InSPEQTER: Infinitesimal Solution of Polynomial Equations by Quadratic Truncation and Elimination Recursion

InSPEQTER$(\{{}^i p_0, {}^i\mathbf{p}, {}^i P\}, d_0^*)$
if length$(\mathbf{p}) = 1$
  Compute $\tilde{c}_{1\pm}$
  return $\{\tilde{c}_{1+}, \tilde{c}_{1-}\}$
else
  Pivoting
  Select best equation i^* and variable j^*
  Permute indices $j^* \leftrightarrow N$ in $\{{}^i p_0, {}^i\mathbf{p}, {}^i P\}$
  for $\pm \in \{\text{sign}({}^{i^*}p_N), -\text{sign}({}^{i^*}p_N)\}$
    Truncation
    Compute $d_{0\pm}, \mathbf{d}_\pm, D_\pm$
    Pruning
    if $|d_{0\pm}| > d_0^*$
      continue
    end if
    Elimination
    Compute $\{{}^i p_0', {}^i\mathbf{p}', {}^i P'\}$ for $i \neq i^*$
    Recursion
    $\{\tilde{\mathbf{c}}\} =$ **InSPEQTER**$(\{{}^i p_0', {}^i\mathbf{p}', {}^i P'\})$
    for $\tilde{\mathbf{c}} \in \{\tilde{\mathbf{c}}\}$
      Compute $\tilde{c}_N$ using $d_{0\pm}, \mathbf{d}_\pm, D_\pm$
      Append $\tilde{c}_N$ to $\tilde{\mathbf{c}}$
      Unpermute indices $j^* \leftrightarrow N$ in $\tilde{\mathbf{c}}$
    end for
    return $\{\tilde{\mathbf{c}}\}$
  end for
end if

all but exceptional circumstances.

3.5 *Solution Refinement*

The InSPEQTER formulation in Algorithm 1 accepts a system of quadratic equations and returns an approximate estimate $\tilde{\mathbf{c}}$ for solutions with small coefficients. The quality of the approximation depends on the solutions proximity to the origin of the state space; the trivial solution can be found exactly, while solutions with elements close to one will be inaccurately estimated. However, if the estimate is closer to the true solution than the latter is to the origin, it can be refined by translating the state space to place the origin at $\tilde{\mathbf{c}}$ and updating the system of equations. Suppose an equation in the original system is

$$p_0^{(0)} + \mathbf{p}^{(0)T}\mathbf{c} + \mathbf{c}^T P^{(0)}\mathbf{c} = 0 \qquad [31]$$

where the superscript (k) indicates the number of refinements the system has gone through. Let $\tilde{\mathbf{c}}^{(0)}$ be the initial estimate for a solution to the system. Making the substitution $\mathbf{c} = \tilde{\mathbf{c}}^{(0)} + \mathbf{\Delta c}$ in Equation 31 leads to the modified system

$$p_0^{(1)} + \mathbf{p}^{(1)T}\mathbf{\Delta c} + \mathbf{\Delta c}^T P^{(1)}\mathbf{\Delta c} \qquad [32]$$

with coefficients given by

$$p_0^{(1)} = p_0^{(0)} + \mathbf{p}^{(0)T}\tilde{\mathbf{c}}^{(0)} + \tilde{\mathbf{c}}^{(0)T} P^{(0)}\tilde{\mathbf{c}}^{(0)} \qquad [33]$$

$$\mathbf{p}^{(1)} = \mathbf{p}^{(0)} + \left(P^{(0)} + P^{(0)T}\right)\tilde{\mathbf{c}}^{(0)} \qquad [34]$$

$$P^{(1)} = P^{(0)} \qquad [35]$$

Solutions to Equation 32 for the new state vector $\mathbf{\Delta c}$ represent small corrections to $\tilde{\mathbf{c}}$ to produce a more accurate solution to the original system. Because the relationship between $\mathbf{c}$ and $\mathbf{\Delta c}$ is affine, the transformation from Equation 31 to Equation 32 is exact and no higher-order terms need to be truncated.

Once an estimate $\mathbf{\Delta}\tilde{\mathbf{c}}$ is obtained from the modified system with $k = 1$, an updated estimate for the original system is obtained from $\tilde{\mathbf{c}}^{(1)} = \tilde{\mathbf{c}}^{(0)} + \mathbf{\Delta}\tilde{\mathbf{c}}$. This process can be repeated for $k = 2, 3, \ldots$, until $\mathbf{\Delta}\tilde{\mathbf{c}}$ is smaller than some value or the residual values $p_0^{(0)} + \mathbf{p}^{(0)T}\tilde{\mathbf{c}}^{(k)} + \tilde{\mathbf{c}}^{(k)T} P^{(0)}\tilde{\mathbf{c}}^{(k)}$ stop decreasing. Figure 4 demonstrates the convergence of the InSPEQTER algorithm for the same 10,000 randomly-generated systems examined in Figure 3. Data are shown for $k = 0, 1$, and 3 refinements, with $d_0^* = 0.5$. As in the preceding section, the systems consist of six quadratic equations in six unknowns. The data are plotted against the ∞-norm of the true solution $\mathbf{c}$, i.e. its coordinate with the largest absolute value, with the 2-norm of the estimation error on the vertical axis. In addition to the raw data, the figure shows the mean and standard deviation over a sliding window of 500 trials. The error in the initial estimate has a slope of 3 on the log-log plot, indicating cubic error growth. This is precisely what would be expected given the truncation of third- and higher-order terms in the derivation of the algorithm. After just one refinement, most scenarios with $|c_i| < 10^{-2}$ have converged to numerical precision. Two more refinement iterations lead to a clear separation between those solutions which have converged and those that are not improving substantially from the initial estimate. The latter category is characterized by $\|\mathbf{c}\|_\infty > 0.1$. The results in Figure 4 inspire confidence in the InSPEQTER algorithm's applicability to the angles-only IROD system in Equation 6, wherein $\|\mathbf{c}\|_\infty$ is typically expected to be between 10^{-3} and 10^{-2}.

While refinement could be considered an essential step for obtaining a solution from InSPEQTER,

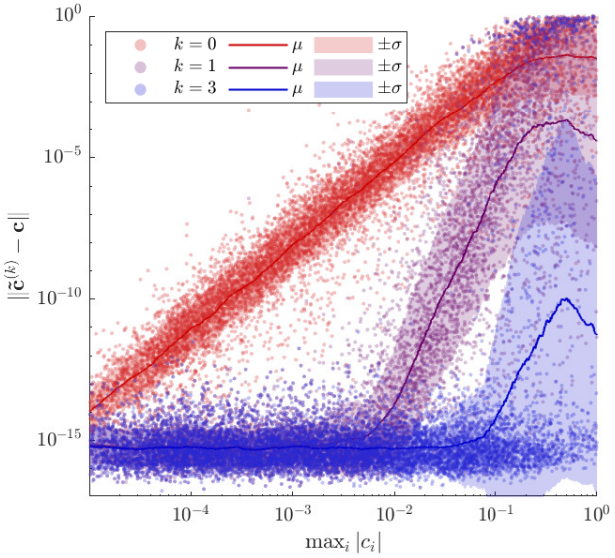

Fig. 4: Error in InSPEQTER estimate $\tilde{\mathbf{c}}$ after $k = 0$, 1, and 3 refinements, as a function of the largest element of the true state $\mathbf{c}$.

it has been omitted from Algorithm 1 for two reasons. First, it should not be included in the recursion step so that computational resources are not wasted finding precise solutions to approximate systems of equations at intermediate steps. Rather it provides a means of improving the output of a complete recursion by repeated application of the algorithm. Second, the definition of the refinement equations may differ from that given in Equations 32 through 35 if higher-order terms have been truncated from the original system. Such a case is discussed in Section 4.2. As a final note, the InSPEQTER algorithm has been developed in this paper in the context of finding solutions close to zero. The refinement procedure demonstrates that the approach can be used to find any solution given a sufficiently close initial estimate. In that context it resembles iterative root-finding methods like generalized Newton-Raphson, but it is readily distinguished from the latter by its ability to find roots given another root as the starting point. This is precisely the situation for angles-only IROD, the topic of the next section.

4. IROD Application

4.1 *Ideal Measurements*

Section 3 introduced a numerical strategy for solving a broad class of problems involving systems of second-order equations. This section demonstrates the use of this method for the problem formulated in Section 2, estimating the relative state of a target spacecraft from a series of line-of-sight measurements. For the initial validation tests, it is assumed that measurements are exact, that the observer has accurate knowledge of its own state, and that non-Keplerian perturbations are negligible. Section 4.2 will show how the approach can be modified to account for systematic errors such as a bias in the measurements.

Figures 1 and 5 illustrate IROD results for a near-circular and elliptical scenario, respectively, obtained by applying Algorithm 1 to Equation 6. The observer's absolute state and observation parameters for these scenarios are given in Table 1. To give physically realistic orbits for the two eccentricity values, the orbit size is characterized by the perigee altitude. Measurements are obtained at five-minute intervals, with the first being taken when the observer's true anomaly is f_0. Both figures show the true trajectory of the target in the observer's RTN frame in black. The three line-of-sight measurements are depicted as blue lines from the observer at the origin to the target's position at the observation times. The red trajectory propagates the estimated state using the second-order ROE model described in Section 2.2, which provided the coefficients for the IROD constraint equations. In both near-circular and eccentric cases the estimated and true trajectories match closely, demonstrating the algorithm's successful determination of the ROE state. In particular, the nonlinear dynamics model provided sufficient information to estimate the separation between observer and target to within the resolution of the figures, without direct range measurements.

Table 1: Scenario definition for validation examples

Scenario	Near-Circular	Elliptical
h_p	750 km	750 km
e	0.0001	0.7321
i	98°	98°
Ω	30°	30°
ω	30°	30°
f_0	20°	20°
Δt	300 s	300 s

While Figures 1 and 5 provide qualitative confirmation of the estimation accuracy, a quantitative assessment is given by examining the metric

$$\epsilon = \frac{\|\delta\tilde{\boldsymbol{\alpha}} - \delta\boldsymbol{\alpha}\|}{\|\delta\boldsymbol{\alpha}\|} \qquad [36]$$

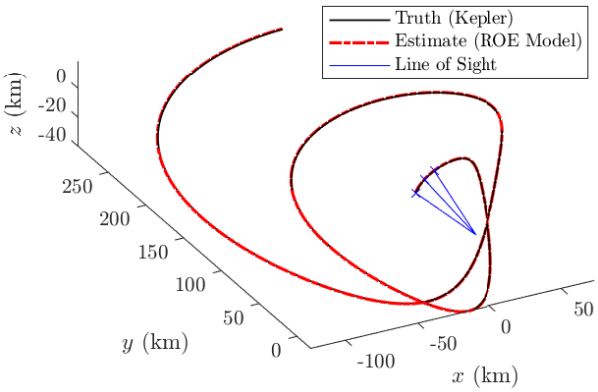

Fig. 5: IROD using InSPEQTER algorithm with $e = 0.73$ and $a\boldsymbol{\delta\alpha} = [-5, 10, 20, 5, 40, 6]^T$ km.

This quantity represents the magnitude of the estimation error normalized by the magnitude of the true relative state. Figure 6 shows result statistics for 10,000 relative motion scenarios with orbit eccentricities drawn from a uniform distribution between 0 and 1. Elements of the relative state vector $a\boldsymbol{\delta\alpha}$ are sampled from the standard normal distribution, with the whole vector scaled by a factor logarithmically distributed between $10^{2.5}$ and $10^{4.5}$ m. Thus, the initial separation between observer and target ranges from a few hundred meters up to a few hundred kilometers. The true anomaly of the initial observation is drawn from a uniform distribution over the orbit period while the measurement interval is randomly selected as a fraction of an orbit between 0 and 0.25. The observer's remaining orbit parameters are pulled from Table 1. These scenarios correspond to those used in the authors' prior examination of the WLD model for IROD using homotopy continuation. [23]

The top of Figure 6 shows the distribution of ϵ for the initial estimate $\boldsymbol{\delta\tilde{\alpha}}$ produced by the InSPEQTER algorithm, as well as for the final estimate obtained after several refinement iterations. For this set of scenarios, the initial estimate gave a median value of ϵ close to 10^{-3}, representing approximately 0.1% relative error. As expected, the distribution of final estimates is shifted towards lower values of the error metric, with a median value of ϵ around $10^{-3.5}$. Less than 2% of scenarios led to initial estimates with $\epsilon > 0.1$, and this fraction is cut in half for the final estimate.

The lower plot of the figure shows the number of refinement iterations required for convergence, with less than 30% of scenarios taking more than two iterations. In contrast to the results of Figure 4, refinement did not converge to the true solution to within numerical precision. Whereas the assessment in Section 3.5 used a system of polynomials constructed around a specified solution, the IROD system considered here combines measurements obtained from a Keplerian propagation with a model which approximates these dynamics to second-order. This means that the true relative state will not exactly solve the system of constraints in Equation 6. Given this fundamental limitation and the accuracy of the initial estimates, a practical implementation of the algorithm could limit the number of refinement iterations to reduce computational effort.

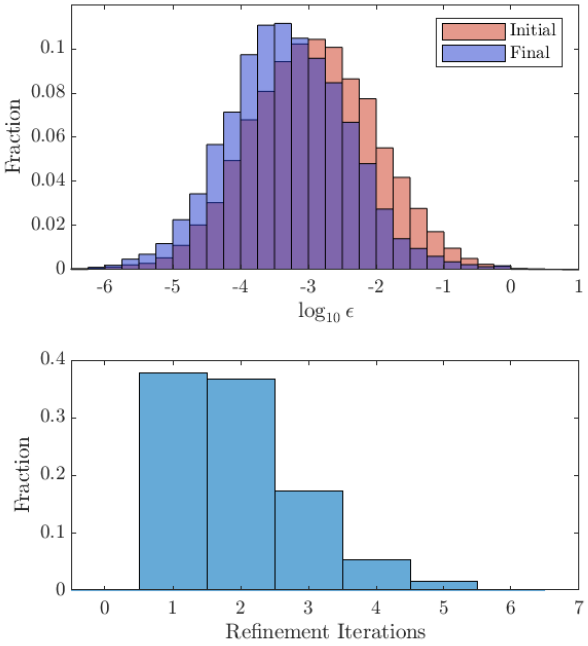

Fig. 6: Distributions of IROD estimation error (top) and required number of refinement iterations (bottom).

Figure 7 shows how the estimation error correlates with the measurement range and orbit eccentricity across the scenarios tested. The top plot shows the raw values of ϵ for each trial, along with the logarithmic moving mean μ and standard deviation σ, as functions of the maximum range across the three measurement times. Small state parameters and therefore small separations are fundamental assumptions of both the second-order dynamics model and the InSPEQTER algorithm. Thus, the overall positive correlation between range and error is to be expected. The large deviations from the mean behav-

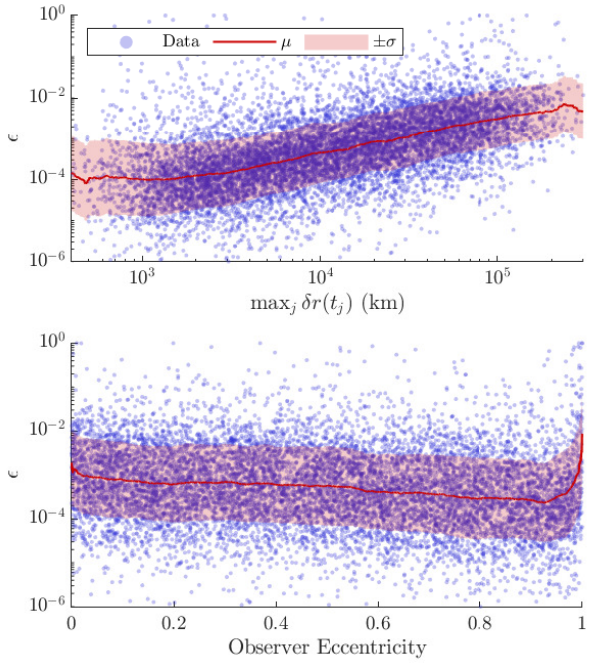

Fig. 7: IROD estimation error as a function of maximum observation distance (top) and observer orbit eccentricity (bottom).

ior suggest that other factors significantly affect the algorithm's performance. The lower half of Figure 7 shows that orbit eccentricity is a weak predictor of estimation error except for nearly parabolic orbits. The small improvement in ϵ with increasing eccentricity can be attributed to the scenario definitions, which linked the eccentricity to the relative state parameters via the orbit radius; higher eccentricity scenarios tend to have smaller ROE and better fit the assumptions of the dynamics model and solution algorithm. The sharp increase in mean error at high eccentricities reflects the invalidity of the dynamics model for parabolic trajectories.

4.2 *Estimating Measurement Bias*

The results of section 4.1 prove the concept of solving the angles-only IROD constraint equations using the second-order ROE model and InSPEQTER algorithm. However, the assumptions of perfect measurements, observer state knowledge, and Keplerian dynamics weakly approximate a realistic orbit scenario. Perturbations in the space environment, biases in the observer's own state estimate, and noise in the bearing-angle measurements all corrupt the idealized problem considered before and pose challenges for the proposed approach. Each of these may be addressed at a different level in the IROD architecture. Perturbations and noise are most appropriately handled at the dynamics modeling and state filtering levels, respectively, which are outside the scope of this work. However, errors which affect the measurements in a systematic way can be addressed within the proposed algorithmic framework.

Biased measurements could arise from error in the observer's absolute orbit or attitude state or in the camera configuration. These would affect the relationship between the camera frame and RTN frame, effectively causing a rotation of the line-of-sight vector. The true line-of-sight vector in RTN $\hat{\boldsymbol{\ell}}$ is related to the measured vector $\hat{\boldsymbol{\ell}}'$ by

$$\hat{\boldsymbol{\ell}} = R(\phi_1, \phi_2, \phi_3)\hat{\boldsymbol{\ell}}' \qquad [37]$$

where $R(\phi_1, \phi_2, \phi_3)$ a rotation matrix formed from an Euler angle sequence with angles ϕ_1, ϕ_2, and ϕ_3 about the $\hat{\mathbf{x}}$, $\hat{\mathbf{y}}$, and $\hat{\mathbf{z}}$ axes. For the purposes of this development, assume the bias affects only the first and third axes and $\phi_2 = 0$. Then for small angles, the rotation matrix is approximated by

$$R_{123}(\phi_1, 0, \phi_3) \approx \begin{bmatrix} 1 & \phi_3 & 0 \\ -\phi_3 & 1 & \phi_1 \\ 0 & -\phi_1 & 1 \end{bmatrix} \qquad [38]$$

Combining Equations 37 and 38 and substituting the resulting components of $\hat{\boldsymbol{\ell}}$ into Equation 2 leads to a new set of constraints relating the measurement $\hat{\boldsymbol{\ell}}'$ to the relative position $\boldsymbol{\delta\bar{\mathbf{r}}}$,

$$\begin{aligned} \left(\ell'_z - \phi_1\ell'_y\right)\bar{y} - \left(\ell'_y - \phi_3\ell'_x + \phi_1\ell'_z\right)\bar{z} &= 0 \\ \left(\ell'_x + \phi_3\ell'_y\right)\bar{z} - \left(\ell'_z - \phi_1\ell'_y\right)\bar{x} &= 0 \\ \left(\ell'_y - \phi_3\ell'_x + \phi_1\ell'_z\right)\bar{x} - \left(\ell'_x + \phi_3\ell'_y\right)\bar{y} &= 0 \end{aligned} \qquad [39]$$

Using the second-order ROE model for $\boldsymbol{\delta\bar{\mathbf{r}}} = [\bar{x}, \bar{y}, \bar{z}]^T$ gives rise to a system of equations with first-order terms in $\delta\alpha_i$, second-order terms in $\delta\alpha_i\delta\alpha_j$ as well as $\delta\alpha_i\phi_j$, and third-order terms in $\delta\alpha_i\delta\alpha_j\phi_k$. Because ϕ_1 and ϕ_3 are assumed to be small, the third-order terms are dropped. What remains is a system in the form of Equation 6, with $\mathbf{c} = [\boldsymbol{\delta\alpha}^T, \phi_1, \phi_3]^T$ and coefficients modified from the definitions in Equation 7 to match the new terms in Equation 2.

Although the system with bias is quadratic, it does not have a form suitable for blind application of the InSPEQTER algorithm. Recall that the derivation in Section 3.2 required that $p_{NN} \neq 0$ and the discriminant be nonzero. The new system with N as index

for the bias angles fails both requirements because $p_{NN} = 0$ and $p_N = 0$. In effect, the biased constraint equations cannot be expressed as quadratic polynomials in the angles ϕ_1 and ϕ_2 with the form of Equation 17. Nor will they generally be able to deeper in the recursion tree. However, near the end of the recursion the equations of the system will take the form

$$p_0 + p_1 c_1 + p_{11} c_1^2 + p_{12} c_1 c_2 = 0 \qquad [40]$$

where c_1 is one of the ROE and c_2 is one of the bias angles. Solving for c_2 leads to

$$c_2 = -\frac{p_0}{p_{12} c_1} - \frac{p_1}{p_{12}} - \frac{p_{11}}{p_{12}} c_1 \qquad [41]$$

It is clear that in the common case that $p_0 = 0$ this expresses c_2 as a linear function of c_1. Even in the more general case, it may be used to eliminate c_2 from a second equation with the form of Equation 40. Multiple unknowns with the form of c_2 may be handled in the same manner and eliminated one at a time. The recursion then terminates with the quadratic equation

$$\left(q_0 - \frac{q_{12}}{p_{12}} \right) + \left(q_1 - \frac{q_{12}}{p_{12}} \right) c_1 + \left(q_{11} - \frac{q_{12}}{p_{12}} \right) c_1^2 = 0 \qquad [42]$$

Thus, InSPEQTER can be modified to handle biases by the addition of an **else if** condition between lines 4 and 5 of Algorithm 1.

The solution refinement strategy introduced in Section 3.5 assumed that the initial system of second-order equations represented the complete description of the system. In this case, it would be possible to incorporate the third-order terms that were truncated from Equation 39 into the definition of the refinement equations. However, this still follows the linearization of the rotation matrix. A conceptually simpler and more effective strategy would be to apply the nonlinear rotation of Equation 37 to the measured line-of-sight vectors using the estimated bias angles, then reconstruct the system of constraints in Equation 39 using the same dynamics model coefficients. Refinements then give corrections to a better approximation of the system.

The effectiveness of the modified InSPEQTER algorithm and refinement strategy on the constraint system with modeled bias was tested on the same 10,000 scenarios examined in Section 4.1. Measurements in each scenario were rotated about two axes by bias angles pulled from a logarithmically uniform distribution between 10^{-5} and 10^{-2} radians, a range from 0.2" to 0.6°, with random sign. Figure 8 shows the resulting error distribution when bias was neglected and modeled in the system. The former case relied on six equations formed from three measurements, as in the results of the preceding section. The system with bias modeled included two additional equations from a fourth line-of-sight measurement to resolve the two bias angles appended to the state. Thus, the results demonstrate not only the modeling of bias but the application of InSPEQTER to a larger system. As in Equation 36, the error metric ϵ is computed using only the ROE portion of the estimated state $\tilde{\mathbf{c}} = [\tilde{\boldsymbol{\delta\alpha}}^T, \tilde{\phi}_1, \tilde{\phi}_2]^T$.

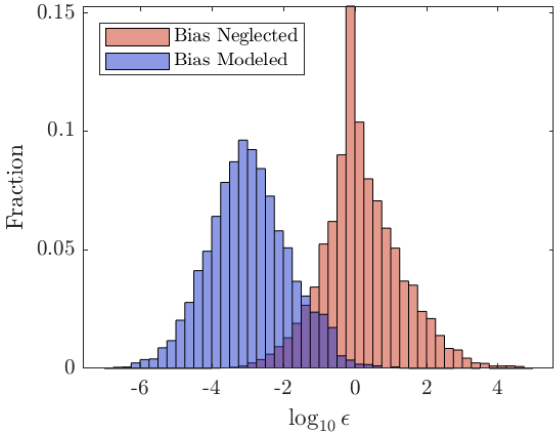

Fig. 8: IROD estimation error when neglecting and modeling bias in the measurements.

The most striking feature of Figure 8 is the sharp peak and symmetry of the bias-neglected distribution about $\epsilon = 10^0$. This highlights the sensitivity of the system both to error in the measurement model and to the trivial solution, for which $\epsilon = 1$. The latter results from the fact that the constraint equations have no 0^{th}-order terms and therefore admit zero as a solution. Modeling the measurement bias leads to a dramatic improvement in accuracy, effectively recovering the error distribution shown in Figure 6 for the case of ideal measurements. The most notable difference is a small increase in the frequency of scenarios having $\epsilon > 10^{-2}$. Further insights are provided by Figure 9, which shows the sensitivity of the estimated state to the largest bias angle. Most of the scenarios with bias modeled having $\epsilon > 10^{-2}$ occur for bias angles greater than 10 arcminutes. Although results for both sets of tests show a positive correlation with

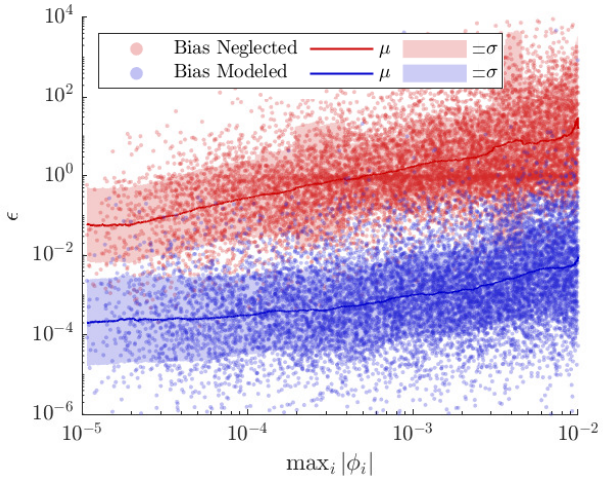

Fig. 9: Sensitivity of IROD estimation error to angular bias in the measurements.

the largest rotation angle, the logarithmic scale of the vertical axis downplays the three orders-of-magnitude difference in moving mean errors. Finally, the figure clearly illuminates the tendency of the system to converge to the trivial solution when bias is neglected.

This section developed the bias model for a constant two-axis rotation of the line-of-sight vectors so that the system could be solved with one additional observation. With the addition of two or three observations, the approach could be extended to include constant drift rates and rotation about a third axis. The pruning strategy described in Section 3.4 is essential for practically implementing such large measurement models; doubling the number of constraint equations from 6 to 12 increases the number of branches in the recursion tree from 64 to 4096.

5. Conclusions

This paper explored the problem of initial relative orbit determination from a sequence of bearing-angle measurements using a polynomial model of the relative motion. It approached this classic problem with two new tools. The first is a second-order mapping from quasi-nonsingular relative orbit elements to position coordinates in the observer spacecraft's RTN frame. By approximating the exact geometric transformations from ROE to the Cartesian relative state, it is more stable over time than higher-order models derived from approximations of the translational state dynamics. Furthermore, its state parameterization provides a direct connection to the large body of literature on GNC and perturbed dynamics in ROE space. Using this second-order model, the fundamental IROD problem becomes one of solving a system of six quadratic constraint equations in the six ROE. The second contribution of this work is the introduction of an efficient algorithm for solving the system of equations. The approach leverages the small magnitude of the ROE state constants and inexact nature of the constraint equations to approximately solve the system of equations by truncating expansions of the quadratic formula at second order and recursively eliminating unknowns from the system. This Infinitesimal Solution of Polynomial Equations by Quadratic Truncation and Elimination Recursion (InSPEQTER) algorithm is bolstered by strategies for pivoting equations and unknowns to reduce approximation errors, pruning the solution tree to reduce computational cost, and iteratively refining the solution to improve accuracy.

Despite the inexact nature of the constraint equations, the algorithm was demonstrated to work well for the IROD problem under idealized assumptions of Keplerian dynamics and perfect observer state and measurement knowledge. Typical relative errors on the order of 10^{-3} were computed for scenarios in the domain of interest. Past work by the authors achieved comparable accuracy using a similar dynamics model to construct the constraint equations and the more rigorous and costly method of homotopy continuation to solve them. Given the validation assumptions, the results represent the limits of achievable accuracy. In practice, the effects of unmodeled forces on the satellite motion and errors in the line-of-sight measurements would impinge on the algorithm's performance. The sensitivity to bias in the measurements was addressed herein by linearizing a small-angle rotation of the line-of-sight vectors, incorporating the resulting second-order effects into the constraint equations, and adding the rotation angles to the state vector. Increasing the size of the state increases the number of equations to solve and overall computational cost, but was shown to reduce errors in the resulting estimates by three orders of magnitude.

As a first application of the InSPEQTER algorithm and second-order ROE mapping to the IROD problem, this work successfully demonstrated their feasibility and opened several doors for future research. One avenue to consider would be a third-order InSPEQTER variant based on the cubic formula. However, this path leads to higher computational complexity and a more expansive solution tree, with little improvement in accuracy expected. More

promising directions point to increasing robustness to noisy measurements, observer state uncertainty, and perturbing forces. The latter can be addressed in part at the level of the dynamics model, with minimal modification to the overall approach. Many linear models exist in the literature for describing the effects of perturbations on the ROEs, and these could readily be incorporated into the second-order mapping. While systematic errors can be addressed in a manner similar to that used to estimate biases in this work, random errors may be best addressed at a higher level. Mean and covariance estimates for the relative state may be obtained by applying the approach to a sample of measurements drawn from an uncertainty distribution. The computational penalty of this strategy is offset by the efficiency of the InSPEQTER algorithm compared to more rigorous polynomial system solvers. All of these updates to the algorithmic framework must be matched by modification of the validation framework to include full-force orbit propagation and realistic errors in the observer's state and bearing-angle measurements. Once its robustness has been demonstrated in high-fidelity simulation, the algorithm's efficiency must be proven through testing on a satellite processor. These research paths ultimately converge on the algorithm's integration into an autonomous, angles-only navigation architecture that will reduce the cost and increase the capability of future distributed space missions.

Acknowledgments

This work was supported by the NASA Office of the Chief Technologist's Space Technology Research Fellowship, NASA grant number 80NSSC18K1176. This work was partially sponsored by the Air Force Office of Scientific Research (AFOSR) and Dr. Michael Yakes via award number FA9550-21-1-0414, for the project titled 'Autonomous Distributed Angles-Only Orbit Determination using Multiple Observers.'

References

[1] D. C. Woffinden and D. K. Geller. Observability criteria for angles-only navigation. *IEEE Transactions on Aerospace and Electronic Systems*, 45(3):1194–1208, 2009.

[2] W. H. Clohessy and R. S. Wiltshire. Terminal guidance system for satellite rendezvous. *Journal of Guidance, Control, and Dynamics*, 27(9):653–658, 1960.

[3] K. Yamanaka and F. Ankersen. New state transition matrix for relative motion on an arbitrary elliptical orbit. *Journal of Guidance, Control, and Dynamics*, 25(1):60–66, 2002.

[4] Simone D'Amico and Oliver Montenbruck. Proximity operations of formation-flying spacecraft using an eccentricity/inclination vector separation. *Journal of Guidance, Control, and Dynamics*, 29(3):554–563, 2006.

[5] Hanspeter Schaub. Relative orbit geometry through classical orbit element differences. *Journal of Guidance, Control, and Dynamics*, 27(5):839–848, 2004.

[6] D. C. Woffinden and D. K. Geller. Optimal orbital rendezvous maneuvering for angles-only navigation. *Journal of Guidance, Control, and Dynamics*, 32(4):1382–1387, 2009.

[7] D. K. Geller and I. Klein. Angles-only navigation state observability during orbital proximity operations. *Journal of Guidance, Control, and Dynamics*, 37(6):1976–1983, 2014.

[8] D. K. Geller and T. A. Lovell. Angles-only initial relative orbit determination performance analysis using cylindrical coordinates. *Journal of Astronautical Sciences*, 64:72–96, 2017.

[9] J. Sullivan and S. D'Amico. Nonlinear kalman filtering for improved angles-only navigation using relative orbital elements. *Journal of Guidance, Control, and Dynamics*, 40(9):2183–2200, 2017.

[10] A. W. Koenig and S. D'Amico. Observability-aware numerical algorithm for angles-only initial relative orbit determination. AAS/AIAA Astrodynamics Specialist Conference, South Lake Tahoe, CA, August 9-13, 2020.

[11] A. W. Koenig, T. Guffanti, and S. D'Amico. New state transition matrices for relative motion of spacecraft formations in perturbed orbits. AAS/AIAA Astrodynamics Specialist Conference, Long Beach, CA, September 13-16, 2016.

[12] T. Guffanti and S. D'Amico. Linear models for spacecraft relative motion perturbed by solar radiation pressure. *Journal of Guidance, Control, and Dynamics*, 42(9):1962–1981, 2019.

[13] J. Sullivan, T. A. Lovell, and S. D'Amico. Angles-only navigation for autonomous on-orbit space situational awareness applications. AAS/AIAA Astrodynamics Specialist Conference, Snowbird, UT, August 19-23, 2018.

[14] H. S. London. Second approximation to the solution of the rendezvous equations. *AIAA Journal*, 1(7):1691–1693, 1963.

[15] M. L. Anthony and F. T. Sasaki. Rendezvous problem for nearly circular orbits. *AIAA Journal*, 3(7):1666–1673, 1965.

[16] M. T. Stringer, B. A. Newman, T. A. Lovell, and A. Omran. Analysis of a new nonlinear solution of relative orbital motion. 23rd International Symposium on Space Flight Dynamics, Pasadena, California, October 29-November 2, 2012.

[17] B. A. Newman, A. J. Sinclair, T. A. Lovell, and A. Perez. Comparison of nonlinear analytical solutions for relative orbital motion. AAS/AIAA Astrodynamics Specialist Conference, San Diego, California, August 4-7, 2014.

[18] R. G. Melton. Time-explicit representation of relative motion between elliptical orbits. *Journal of Guidance, Control, and Dynamics*, 23(4):604–610, 2000.

[19] E. A. Butcher, E. Burnett, and T. A. Lovell. Comparison of relative orbital motion perturbation solutions in cartesian and spherical coordinates. 27th AAS/AIAA Space Flight Mechanics Meeting, San Antonio, TX, February 5-9, 2017.

[20] E. A. Butcher, E. Burnett, J. Wang, and T. A. Lovell. A new, time-explicit j2-perturbed nonlinear relative orbit model with perturbation solutions. AAS/AIAA Astrodynamics Specialist Conference, Stevenson, WA, August 20-24 2017.

[21] M. Willis, T. A. Lovell, and S. D'Amico. Second order analytical solution for relative motion on arbitrarily eccentric orbits. 29th AAS/AIAA Space Flight Mechanics Meeting, Ka'anapali, Maui, Hawaii, January 13-17, 2019.

[22] T. Henderson, T. A. Lovell, A. Sizemore, K. Horneman, and D. Zuehlke. Initial relative orbit determination solutions using polynomial systems. 29th AAS/AIAA Space Flight Mechanics Meeting, Ka'anapali, Maui, HI, January 13-17, 2019.

[23] M. Willis and S. D'Amico. Applications and limitations of angles-only relative navigation using polynomial solutions. AAS/AIAA Astrodynamics Specialist Conference, Virtual, August 9-13, 2020.

[24] J. Sullivan, S. Grimberg, and S. D'Amico. Comprehensive survey and assessment of spacecraft relative motion dynamics models. *Journal of Guidance, Control, and Dynamics*, 40(8):1837–1859, 2017.

[25] On the theories of triangular sets. *Journal of Symbolic Computation*, 28(1):105–124, 1999.

[26] I. Stewart. *Galois Theory*. Chapman Hall/CRC, 3rd edition, 2004.

[27] B. Newman, T. A. Lovell, E. Pratt, and E. Duncan. Quadratic hexa-dimensional solution for relative orbit determination. AAS/AIAA Astrodynamics Specialist Conference, San Diego, CA, August 4-7, 2014.

[28] T. A. Lovell, K. Horneman, A. Sizemore, and B. Morton. Angles only initial orbit determination: Comparison of relative dynamics and inertial dynamics approaches with error analysis. 28th AAS/AIAA Space Flight Mechanics Meeting, Kissimmee, FL, January 8-12, 2018.

[29] D. J. Bates, J. D. Hauenstein, A. J. Sommese, and C. W. Wampler. *Numerically Solving Polynomial Systems with Bertini*. SIAM, 2013.

[30] J. Kruger and S. D'Amico. Autonomous angles-only multi-target tracking for spacecraft swarms. AAS/AIAA Astrodynamics Specialist Conference, South Lake Tahoe, CA, August 9-13, 2020.

[31] D. Zuehlke, T. Henderson, T. A. Lovell, and A. Sizemore. An end-to-end process for local space situational awareness from optical observers. IEEE/ION Position, Location and Navigation Symposium (PLANS), Portland, OR, April 20-23, 2020.

[32] A. McLennan. The expected number of real roots of a multihomogeneous system of polynomial equations. *American Journal of Mathematics*, 124(1):49–73, 2002.

Appendix: Mapping from ROE to RTN coordinates

The second-order mapping from relative orbit elements $\boldsymbol{\delta\alpha}$ to normalized relative position coordinates $\boldsymbol{\delta\bar{\mathbf{r}}} = \boldsymbol{\delta\mathbf{r}}/r = [\bar{x}, \bar{y}, \bar{z}]^T$ may be expressed as

$$\bar{x} = \mathbf{b}_x(\theta)^T \boldsymbol{\delta\alpha} + \boldsymbol{\delta\alpha}^T B_x(\theta) \boldsymbol{\delta\alpha}$$
$$\bar{y} = \mathbf{b}_y(\theta)^T \boldsymbol{\delta\alpha} + \boldsymbol{\delta\alpha}^T B_y(\theta) \boldsymbol{\delta\alpha}$$
$$\bar{z} = \mathbf{b}_z(\theta)^T \boldsymbol{\delta\alpha} + \boldsymbol{\delta\alpha}^T B_z(\theta) \boldsymbol{\delta\alpha}$$

where $\mathbf{b}_i \in \mathbb{R}^6$ are vectors containing the time varying coefficients of the first-order mapping and $B_i \in \mathbb{R}^{6\times6}$ are triangular matrices containing the time-varying coefficients of the second-order terms. To simplify notation, the coefficients are expressed in terms of the constant $\eta = \sqrt{1-e^2}$ and time-varying quantities

$$k = \frac{a\eta^2}{r} = 1 + e_x \cos\theta + e_y \sin\theta$$
$$k' = \frac{dk}{d\theta} = -e_x \sin\theta + e_y \cos\theta$$

where $\theta = \omega + f$ is the true argument of latitude. Mappings to relative velocity can be obtained from the derivatives of the coefficients, taking care to apply the chain rule to $\dot{r}$.

First-Order Coefficients

Given the ROE at a point in time, the concurrent relative position is approximated from the first order mapping $\boldsymbol{\delta\bar{\mathbf{r}}} = [\mathbf{b}_x, \mathbf{b}_y, \mathbf{b}_z]^T \boldsymbol{\delta\alpha}$. The nonzero coefficients for the radial motion are

$$b_{x,1} = 1$$
$$b_{x,2} = -\frac{kk'}{\eta^3}$$
$$b_{x,3} = -\frac{k}{\eta^3}\left[\cos\theta + e_x\left(\frac{1-k}{1+\eta}\right)\right]$$
$$b_{x,4} = -\frac{k}{\eta^3}\left[\sin\theta + e_y\left(\frac{1-k}{1+\eta}\right)\right]$$
$$b_{x,6} = \frac{kk'}{\eta^3}\cot i$$

The nonzero coefficients for the transverse motion are

$$b_{y,2} = \frac{k^2}{\eta^3}$$
$$b_{y,3} = \frac{1}{\eta^2}\left[(1+k)\sin\theta + e_y\frac{k^2}{\eta}\left(\frac{e_y}{1+\eta}\right)\right]$$
$$b_{y,4} = -\frac{1}{\eta^2}\left[(1+k)\cos\theta + e_x\frac{k^2}{\eta}\left(\frac{e_x}{1+\eta}\right)\right]$$
$$b_{y,6} = \left(1 - \frac{k^2}{\eta^3}\right)\cot i$$

Finally, the nonzero coefficients for the out-of-plane motion are simply

$$b_{z,5} = \sin\theta$$
$$b_{z,6} = -\cos\theta$$

Second-order Coefficients

In total, B_x, B_y, and B_z contain 41 nonzero elements out of 63 possible given their upper-triangular structure. Ten of these are reused from the first-order mapping. To streamline the second-order mapping, the trigonometric functions $\cos\theta$, $\sin\theta$, and $\cot i$ should be precomputed. Additionally, it will be helpful to define the recurring quantities

$$C = \frac{e_x + \cos\theta}{\eta^2} \qquad S = \frac{e_y + \sin\theta}{\eta^2}$$

$$\kappa_1 = \frac{k}{\eta} \qquad \kappa_2 = \frac{\kappa_1}{\eta} \qquad \kappa_3 = \frac{\kappa_2}{\eta}$$
$$\kappa' = -\frac{k'}{k} \qquad \varepsilon_x = \frac{e_x}{1+\eta} \qquad \varepsilon_y = \frac{e_y}{1+\eta}$$

The second-order out-of-plane coefficients are then

$$B_{z,15} = \sin\theta$$
$$B_{z,16} = -\cos\theta$$
$$B_{z,25} = C\kappa_1$$
$$B_{z,26} = S\kappa_1$$
$$B_{z,35} = B_{z,25}\varepsilon_y + S\cos\theta$$
$$B_{z,36} = B_{z,26}\varepsilon_y + \kappa_2 + S\sin\theta$$
$$B_{z,45} = -B_{z,25}\varepsilon_x - \kappa_2 - C\cos\theta$$
$$B_{z,46} = -B_{z,26}\varepsilon_x - C\sin\theta$$
$$B_{z,56} = -B_{z,25}\cot i$$
$$B_{z,66} = \left(-B_{z,26} + \frac{1}{2}\sin\theta\right)\cot i$$

The second-order transverse coefficients are

$$B_{y,12} = \kappa_1\kappa_2$$
$$B_{y,13} = B_{y,12}\varepsilon_y + S + \kappa_2\sin\theta$$
$$B_{y,14} = -B_{y,12}\varepsilon_x - C - \kappa_2\cos\theta$$
$$B_{y,16} = (1 - B_{y,12})\cot i$$

$$B_{y,23} = B_{y,12}\left(\frac{e_x}{\eta^2} + \frac{\cos\theta}{k}\right)$$
$$B_{y,24} = B_{y,12}\left(\frac{e_y}{\eta^2} + \frac{\sin\theta}{k}\right)$$
$$B_{y,26} = \kappa' B_{y,12}\cot i$$
$$B_{y,33} = \frac{1}{2\eta^2}\left[\varepsilon_x\varepsilon_y B_{y,12}\left(2+3\eta\right) + \left(2e_x + \cos\theta\right)S - \left(1-\eta\right)\varepsilon_y\kappa_2\cos\theta\right]$$
$$B_{y,34} = -\frac{1}{2\eta^2}\left[\left(\varepsilon_x^2 - \varepsilon_y^2\right)B_{y,12}\left(2+3\eta\right) + \kappa_2\left(e_x - 2\varepsilon_x\right)\cos\theta - \kappa_2\left(e_y - 2\varepsilon_y\right)\sin\theta - \left(2e_y + \sin\theta\right)S + \left(2e_x + \cos\theta\right)C\right]$$
$$B_{y,36} = -\kappa_3\left[\varepsilon_x\left(1-k\right) + e_x\kappa_2 + 2\cos\theta\right]\cot i$$
$$B_{y,44} = \frac{-1}{2\eta^2}\left[\varepsilon_x\varepsilon_y B_{y,12}\left(2+3\eta\right) + \left(2e_y + \sin\theta\right)C - \left(1-\eta\right)\varepsilon_x\kappa_2\sin\theta\right]$$
$$B_{y,46} = -\kappa_3\left[\varepsilon_y\left(1-k\right) + e_y\kappa_2 + 2\sin\theta\right]\cot i$$
$$B_{y,55} = -\frac{1}{2}\sin\theta\cos\theta$$
$$B_{y,56} = -\sin^2\theta$$
$$B_{y,66} = -B_{y,55} - B_{y,26}\cot i$$

Last, the second-order radial coefficients are computed in terms of the transverse coordinates as

$$B_{x,12} = \kappa' B_{y,12}$$
$$B_{x,13} = -\kappa_3\left[\cos\theta + \varepsilon_x\left(1-k\right)\right]$$
$$B_{x,14} = -\kappa_3\left[\sin\theta + \varepsilon_y\left(1-k\right)\right]$$
$$B_{x,16} = -B_{x,12}\cot i$$
$$B_{x,22} = -\frac{1}{2}B_{y,12}\kappa_3$$
$$B_{x,23} = -B_{y,12}\left(\kappa_3\varepsilon_y + S\right)$$
$$B_{x,24} = B_{y,12}\left(\kappa_3\varepsilon_x + C\right)$$
$$B_{x,26} = B_{y,12}\left(\kappa_3 - 1\right)\cot i$$
$$B_{x,33} = \frac{S}{\kappa_1^2}\left(B_{y,13} - S\right) - \frac{B_{y,13}^2}{2k} + \kappa' B_{y,33}$$
$$B_{x,34} = \frac{1}{\kappa_1^2}\left(2SC - CB_{y,13} + SB_{y,14}\right) - \frac{B_{y,13}B_{y,14}}{k} + \kappa' B_{y,34}$$
$$B_{x,36} = -\left\{B_{y,12}\left[\varepsilon_y\left(1-\kappa_3\right) - S\right] + S + \kappa_2\sin\theta\right\}\cot i$$
$$B_{x,44} = -\frac{C}{\kappa_1^2}\left(B_{y,14} + C\right) - \frac{B_{y,14}^2}{2k} + \kappa' B_{y,44}$$
$$B_{x,46} = \left\{B_{y,12}\left[\varepsilon_x\left(1-\kappa_3\right) - C\right] + C + \kappa_2\cos\theta\right\}\cot i$$
$$B_{x,55} = -\frac{1}{2}\sin^2\theta$$
$$B_{x,56} = \sin\theta\cos\theta$$
$$B_{x,66} = \frac{1}{2}\left[B_{y,12}\left(2-\kappa_3\right) - 1\right]\cot^2 i - \frac{1}{2} - B_{x,55}$$

Mapping from ROE at reference time

For Keplerian motion, $\delta\lambda$ is the only time-varying ROE. Its value after an elapsed time Δt is related to its initial value by the second-order approximation

$$\delta\lambda = \delta\lambda_0 - \frac{3}{2}n\Delta t\delta a + \frac{15}{8}n\Delta t\delta a^2$$

To propagate the relative position given the ROE at a point in time, it is most efficient to first update $\delta\lambda$ and then use the coefficients of the second-order mapping given above. However, for IROD it is preferable to combine these steps into a set of coefficients that map from the ROE at an initial time to the relative position at a later time. This modification affects only the coefficients of terms involving δa. The first-order coefficients for $i \in \{x, y, z\}$ transform according to

$$b'_{i,1} = b_{i,1} - \frac{3}{2}n\Delta t b_{i,2}$$

The second-order coefficients are modified according to

$$B'_{i,11} = B_{i,11} + \frac{3}{8}n\Delta t B_{i,12} + \frac{9}{4}n^2\Delta t^2 B_{i,22}$$
$$B'_{i,12} = B_{i,12} - 3n\Delta t B_{i,22}$$
$$B'_{i,1j} = B_{i,1j} - \frac{3}{2}n\Delta t B_{i,2j}$$

where $j \in \{3, 4, 5, 6\}$.